



**Three-dimensional self-assembled SnS<sub>2</sub>-Nano-Dots@Graphene Hybrid Aerogel as an Efficient Polysulfide Reservoir for High-performance Lithium-sulfur Batteries**

Journal:	<i>Journal of Materials Chemistry A</i>
Manuscript ID	TA-ART-02-2018-001089.R1
Article Type:	Paper
Date Submitted by the Author:	22-Mar-2018
Complete List of Authors:	Luo, Liu; University of Texas at Austin, Chemical Engineering Chung, Sheng-Heng; University of Texas at Austin, Materials Science and Engineering Manthiram, Arumugam; University of Texas at Austin, Materials Science and Engineering

## Three-dimensional self-assembled SnS<sub>2</sub>-Nano-Dots@Graphene Hybrid Aerogel as an Efficient Polysulfide Reservoir for High-performance Lithium-sulfur Batteries

Liu Luo, Sheng-Heng Chung, and Arumugam Manthiram\*  
McKetta Department of Chemical Engineering & Texas Materials Institute  
The University of Texas at Austin, Austin, TX 78712, USA  
E-mail: manth@austin.utexas.edu (A. Manthiram)

### Abstract

Reliable sulfur cathodes hold the key to realize high-performance lithium-sulfur (Li-S) batteries, yet the electrochemical inefficiency and instability arising from the poor conductivity of sulfur and lithium sulfide together with polysulfide diffusion remain challenging. We present here a new three-dimensional graphene aerogel embedded with *in-situ* grown SnS<sub>2</sub> nano dots (SnS<sub>2</sub>-ND@G) as an efficient sulfur host. First, benefiting from a highly conductive, hierarchically porous, and mechanically self-supported architecture, the SnS<sub>2</sub>-ND@G aerogel enables the cathode to hold high sulfur content (75 wt.%) and loading (up to 10 mg cm<sup>-2</sup>). Both values exceed most of the reported metal-compound-related cathode work (< 60 wt.% sulfur content and < 3 mg sulfur loading) in the literature. Second, this work takes advantage of a facile one-pot self-assembly fabrication, effectively guaranteeing a homogeneous deposition of SnS<sub>2</sub> nano dots in graphene aerogel with a small amount of SnS<sub>2</sub> (16 wt.%). It greatly overcomes the shortcomings of the physical incorporation methods to make metal-compound/carbon substrates reported in previous studies. More importantly, by rationally combining the physical entrapment from graphene and chemical adsorptivity from SnS<sub>2</sub> nano dots towards polysulfides, the SnS<sub>2</sub>-ND@G aerogel demonstrates remarkably improved polysulfide-trapping capability and electrochemical stability. As a result, a high peak capacity of 1234 mA h g<sup>-1</sup>, a high reversible capacity of 1016 mA h g<sup>-1</sup> after 300 cycles, exceptional rate capability (C/10 – 3C rates), and impressive areal capacity (up to 11 mA h cm<sup>-2</sup>) are achieved. This work provides a viable path to integrate conductive graphene

network and nano-sized SnS<sub>2</sub> as a promising cathode substrate for developing advanced Li-S batteries.

*Keywords:* lithium-sulfur batteries, high-loading cathodes, graphene aerogel, SnS<sub>2</sub> nano-dots, electrochemical performance

## Introduction

The ever-increasing demand for energy in portable electronic devices and electric vehicles calls for advanced rechargeable batteries with significantly improved energy density to compete with the state-of-the-art lithium-ion (Li-ion) batteries. Lithium-sulfur (Li-S) batteries, with an overwhelming theoretical energy density of 2600 W h kg<sup>-1</sup>, hold great promise for next-generation rechargeable battery technology.<sup>1-3</sup> In addition, with the merits of natural abundance, low cost, and environmental friendliness of sulfur, Li-S batteries prevail in terms of cost effectiveness and supply sustainability over conventional Li-ion batteries.<sup>4,5</sup> The practical realization of Li-S batteries, however, is still plagued with critical barriers; the major bottleneck lies in the insulating nature of sulfur (conductivity:  $5 \times 10^{-30}$  S cm<sup>-1</sup>) and its discharge products along with the diffusion of intermediate polysulfides during cycling. Hence, Li-S batteries suffer from low electrochemical utilization, rapid capacity fade, and poor cycle life.<sup>1,4,5</sup>

With an aim to address these issues, optimal cathode materials, multi-functional separators, new electrolyte additives, and anode protection system are being intensively pursued.<sup>1-7</sup> In the studies of cathode configuration, numerous efforts have been focused on carbonaceous materials as effective substrates to encapsulate sulfur species.<sup>8</sup> Among them, graphene has emerged as a prospective candidate because of its high electrical conductivity, high surface area, excellent mechanical flexibility, and good compatibility with other additives.<sup>9-12</sup> Nevertheless, graphene itself has been proved to have weak physical absorption towards polysulfides. This makes it

difficult to be used alone in improving the electrochemical stability of Li-S cells,<sup>11,13</sup> and even hard to build high-loading sulfur cathodes with long cycle life.<sup>14,15</sup>

Transition metal oxides (TiO,<sup>16</sup> TiO<sub>2</sub>,<sup>11</sup> Ti<sub>4</sub>O<sub>7</sub>,<sup>17</sup> MnO<sub>2</sub>,<sup>18</sup> MgO,<sup>19</sup> CuO,<sup>20</sup>), sulfides (CoS<sub>2</sub>,<sup>21</sup> TiS<sub>2</sub>,<sup>22,23</sup> and CuS,<sup>24</sup>), and nitrides (WN, TiN, and VN)<sup>25</sup> have been reported (i) as efficient polysulfide barriers due to the strong chemical bonding with polysulfides for enhanced polysulfide-trapping ability and (ii) for fast reaction capability because of the catalytic effects in increasing the conversion rate of soluble long-chain polysulfides to insoluble short-chain Li<sub>2</sub>S<sub>2</sub>/Li<sub>2</sub>S.<sup>25</sup> However, their conductivity is relatively low with respect to the carbon conductive agent. As a result, constructing hybrid substrates that combine both conductive carbon and transition-metal compounds is a better choice to improve the electrochemical performance of Li-S batteries.<sup>11,15,24</sup> The mostly reported metal sulfides/carbon composites that demonstrated enhanced Li-S cell performance contained above 50 wt. % metal sulfides in the mixtures, in which metal sulfides with large particles were used.<sup>21,26</sup> The high content of metal sulfides and the use of large chunk of the adsorbent agents, however, might greatly lower the conductivity of the mixture and accessible active sites.<sup>25</sup> Accordingly, in order to enhance the function of metal sulfides as an efficient sulfur host in boosting the cell performance, synthesizing small-sized metal sulfides with decreased content in the functional mixtures is crucial to simultaneously guarantee good polysulfide-trapping ability and decent electronic conductivity.<sup>25</sup>

In this regard, we present here a three-dimensional cathode substrate configured with tin disulfide (SnS<sub>2</sub>) nano dots *in-situ* grown in a conductive graphene aerogel as the SnS<sub>2</sub> nano dots@graphene (SnS<sub>2</sub>-ND@G). The (SnS<sub>2</sub>-ND@G) obtained *via* a facile one-pot hydrothermal process exhibits three-dimensional, hierarchically porous architecture, as illustrated in Fig. 1a. This unique structure renders multiple advantages. First, the conductive graphene aerogel

(conductivity:  $2 - 3 \text{ S cm}^{-1}$ ) creates interconnected conductive pathways for fast electron/ion transport, favoring promoted redox kinetics during the charge/discharge processes.<sup>13,27</sup> Second, apart from storing the active material, the porous framework of the graphene aerogel serves as interlinked channels to retain electrolyte and physically localize the soluble polysulfides.<sup>28,29</sup> Third, the uniformly anchored SnS<sub>2</sub> nano dots act as abundant reaction sites to chemically adsorb polysulfides, further suppressing the polysulfide diffusion and minimizing the loss of active material. Fourth, SnS<sub>2</sub> has the layered CdI<sub>2</sub>-type structure where each tier of tin atoms is sandwiched in between double tiers of hexagonally close-packed sulfur atoms.<sup>13,30,31</sup> As a polysulfide adsorbent, the interlayer spacing between adjacent sulfur layers due to the weak Van der Waals interaction is beneficial for fast lithium-ion transfer.<sup>31-34</sup> Finally, such self-supported and elastic architecture is free from the use of extra current collector and binder, and also helps buffer the volume changes during the phase transitions of sulfur. It minimizes the weight of inert additives and ensures the electrode integrity as well during long cycling.<sup>29,35</sup> With these desirable features, the electrochemical utilization of sulfur and cycling stability are significantly improved when applying SnS<sub>2</sub>-ND@G aerogel as the sulfur host with high sulfur content (75 wt. %) and high sulfur loading (up to  $10 \text{ mg cm}^{-2}$ ). Both values exceed the majority of previous sulfur-cathode studies involving metal-sulfides or other metal compounds ( $< 60 \text{ wt.}\%$  sulfur content and  $< 3 \text{ mg}$  sulfur loading), as shown in Fig. 1b. As a result, the promoted high-loading areal capacity is up to 3 times higher than that in the previous studies, as reflected in Fig. 1c (Table S1, ESI).

## Experimental

### Synthesis of SnS<sub>2</sub>-nano-dots@graphene (SnS<sub>2</sub>-ND@G) hybrid aerogel.

Graphene oxide (GO) was synthesized from natural flake graphite by a modified Hummers method. Hydrothermal assembly and freeze-drying procedure were combined to prepare the SnS<sub>2</sub>-

ND@G hybrid aerogel. Typically, 35.1 mg of  $\text{SnCl}_4 \cdot 5\text{H}_2\text{O}$  was dissolved in 60 mL of GO aqueous dispersion ( $3 \text{ mg mL}^{-1}$ ). After magnetic stirring for 30 min, 36.3 mg of L-cysteine was added to the mixture suspension, followed by vigorously stirring and ultrasonication for 30 min. The obtained suspension was then transferred into a 100 ml Teflon-lined stainless steel autoclave and hydrothermally treated at  $190 \text{ }^\circ\text{C}$  for 24 h. After the autoclave was naturally cooled to room temperature, the black hybrid hydrogel was washed with distilled water several times, followed by freeze-drying for 3 days to obtain the  $\text{SnS}_2\text{-ND@G}$  aerogel. The graphene aerogel was prepared in the same procedure without adding  $\text{SnCl}_4 \cdot 5\text{H}_2\text{O}$  and L-cysteine, and was used as a control.

#### **Electrochemical Cell assembly.**

Li-S cells (CR2032 coin cells) were assembled in an Ar-filled glove box. The blank electrolyte added to the Li-metal anode side was 1.85 M  $\text{LiCF}_3\text{SO}_3$  (Acros Organics) and 0.1 M  $\text{LiNO}_3$  (Acros Organics) dissolved in a mixed solvent of dimethoxy ethane (DME, Acros Organics) and 1,3-dioxolane (DOL, Acros Organics) (1 : 1 by volume). The polysulfide catholyte was prepared by mixing sulfur powder (99.5%, Acros Organics) and an appropriate amount of lithium sulfide ( $\text{Li}_2\text{S}$ , 99.9%, Acros Organics) into the blank electrolyte. It was then heated at  $60 \text{ }^\circ\text{C}$  in an Ar-filled glove box for 2 days to give 0.8 M  $\text{Li}_2\text{S}_6$  solution. The as-prepared  $\text{Li}_2\text{S}_6$  catholyte was injected into the manually-compressed  $\text{SnS}_2\text{-ND@G}$  aerogel as cathode. The electrolyte/sulfur (E/S) ratio was controlled to be  $10 \text{ } \mu\text{L}/\text{mg}$ . The cathode and anode were separated by a polypropylene separator (Celgard 2500). The assembled Li-S cells were placed to rest for 30 min before performing the cycling test.

#### **Materials characterization and electrochemical analyses.**

X-ray diffraction (XRD) measurement was conducted with a Miniflex 600 X-ray diffractor with Cu  $\text{K}\alpha$  radiation. Thermogravimetric analysis (TGA) was utilized with a Perkin–Elmer thermal

analysis system under flowing nitrogen from 50 to 800 °C (20 °C min<sup>-1</sup> heating rate) to determine the SnS<sub>2</sub> content in the hybrid aerogel. Porosity analyses were carried out with an automated gas sorption analyzer (AutoSorb iQ2, Quantachrome Instruments) at 77 K. Surface and bonding characterization were conducted with an X-ray photoelectron spectrometer (XPS, Kratos Analytical Company). XPS spectra decomposition was carried out with a CasaXPS program with Gaussian-Lorentzian functions after the subtraction of the Shirley background. All peaks were calibrated based on the C 1s peak at 284.6 eV. UV-visible absorption spectroscopy analysis was performed with a Cary 5000 spectrophotometer with baseline correction (Varian). Microstructure information was characterized with a scanning electron microscope instrument (FEI Quanta 650 FE-SEM). A JEOL 2010F transmission electron microscopy (TEM) was used to conduct structural analysis by high resolution TEM (HRTEM) and elemental mapping with energy dispersive X-ray spectroscopy (EDX). Cyclic voltammetry (CV) measurements were examined with a universal potentiostat (VoltaLab PGZ 402, Radiometer Analytical) at scan rates of 0.05 mV s<sup>-1</sup> in the potential range of 1.7 – 2.8 V. Charge/discharge profiles and cycling performances were carried out with a cell cycler (Arbin Instruments) at 1.7 – 2.8 V at various cycling rates (C/10 – 3C rates). Electrochemical impedance spectroscopy (EIS) profiles were obtained with a potentiostat (VMP3, Bio-logic) in the frequency range of 1 MHz to 100 mHz with an AC voltage amplitude of 5 mV at the open-circuit voltage.

## Results and discussion

The scanning electron microscopy (SEM) images in Fig. 2a – 2c demonstrate that SnS<sub>2</sub>-ND@G aerogel possesses a highly porous, hierarchical architecture. Such structure guarantees abundant storage space to localize the active material and favor the electrolyte access. Meanwhile, as shown in Fig. 2c, SnS<sub>2</sub> nanoparticles with ~ 120 nm in diameter are deposited uniformly on the

wrinkling graphene sheets without obvious aggregations. It is probably ascribed to the interaction between the graphene oxide (GO) surface containing multiple functional groups and the well-dispersed Sn precursor during the initial synthesis of the SnS<sub>2</sub>-ND@G aerogel. Therefore, abundant nucleation sites are provided to induce homogenous growth of SnS<sub>2</sub> nanoparticles during the subsequent hydrothermal reaction.<sup>33</sup> The morphology of SnS<sub>2</sub>-ND@G aerogel is further characterized by transmission electron microscopy (TEM). As shown in Fig. 2d, even after strong ultrasonication during the preparation of TEM samples, the hexagonal SnS<sub>2</sub> nanoparticles are still tightly anchored in the ultrathin graphene layers, confirming a strong adhesion between the *in-situ* grown SnS<sub>2</sub> and graphene.<sup>36</sup> The corresponding energy-dispersive X-ray (EDX) elemental mapping analysis in Fig. 2e further ascertains these nanoparticles in the form of Sn and S elements. Moreover, the high-resolution TEM (HRTEM) image (Fig. 2f) exhibits parallel fringes with a lattice spacing of 0.59 nm, which corresponds to the (001) interplanar distance of SnS<sub>2</sub>.<sup>37,38</sup> It is worth mentioning that Fig. 2g also detects a variety of smaller SnS<sub>2</sub> nano dots (~ 5 nm in diameter) distributed on the graphene sheets (marked as dotted circle). Furthermore, HRTEM image of an individual smaller SnS<sub>2</sub> nano dots in Fig. 2h presents well-resolved crystal lattice with an interplanar spacing of 0.31 nm, which is related to the (100) plane of SnS<sub>2</sub>.<sup>13,36,38</sup> Therefore, it is reasonable to conclude that crystalline SnS<sub>2</sub> nano dots are homogeneously deposited in the SnS<sub>2</sub>-ND@G aerogel, acting as sufficient adsorption sites to minimize polysulfide migration.

Fig. 3a displays X-ray diffraction (XRD) patterns of the as-synthesized SnS<sub>2</sub>-ND@G aerogel, clearly evidencing the successful incorporation of SnS<sub>2</sub> into graphene scaffold. The sharp characteristic peaks of SnS<sub>2</sub> (magnetite, JCPDS No. 23-677) suggest the high crystallinity of hexagonal SnS<sub>2</sub> prepared by this method.<sup>31,33,38</sup> To determine the SnS<sub>2</sub> content in the obtained aerogel, thermogravimetric analysis (TGA) was conducted in air at a heating rate of 20 °C min<sup>-1</sup>,

as shown in Fig. 3b. The initial weight loss below 200 °C is due to the removal of absorbed water.<sup>13,31</sup> The second weight loss between 200 and 400 °C is mainly attributed to the phase transformation from SnS<sub>2</sub> to SnO<sub>2</sub>.<sup>31,33</sup> The last weight loss above 400 °C results from the decomposition of graphene and further oxidation of SnS<sub>2</sub> into SnO<sub>2</sub>.<sup>31,38</sup> From Fig. 3b, the weight fraction of SnS<sub>2</sub> in the SnS<sub>2</sub>-ND@G aerogel calculated from the residual SnO<sub>2</sub> (~ 13 wt.%) is 16 wt.%. With such a relatively low content of SnS<sub>2</sub>, the resulting SnS<sub>2</sub>-ND@G aerogel still preserves high porosity as shown in Fig. 3c.<sup>31,39</sup> Accordingly, the Brunauer–Emmett–Teller (BET) specific surface area of the SnS<sub>2</sub>-ND@G aerogel is 132 m<sup>2</sup> g<sup>-1</sup> with the pore size mainly distributed from 3 to 10 nm (~ 1.5 nm in average) *via* the arrett–Joyner–Halenda (BJH) method. As a reference, the specific surface area of graphene aerogel is 120 m<sup>2</sup> g<sup>-1</sup> with an average pore size of 3 nm (Fig. 3d). The relatively high specific surface area and numerous hierarchical pores in the SnS<sub>2</sub>-ND@G aerogel are beneficial for fast Li<sup>+</sup> diffusion and electrolyte access during repeated cycling.<sup>30,31</sup>

On the other hand, the X-ray photoelectron spectroscopy (XPS) survey spectrum (Fig. S3, ESI) detects the presence of Sn, S, and C components in the SnS<sub>2</sub>-ND@G aerogel, which is consistent with the XRD result. In particular, the high-resolution C 1s XPS spectrum of GO (Fig. 4a) displays four peaks at 284.6, 286.6, 288.1, and 288.8 eV representing, respectively, C–C/C=C, C–O, C=O, and O–C=O bonding.<sup>30,40</sup> As expected, the peak intensity ratio of these oxygen-containing functional groups to C–C/C=C bonding in SnS<sub>2</sub>-ND@G aerogel is much lower than that in the GO samples (Fig. 4b), in good line with the above-mentioned XPS survey result. Such comparison clearly indicates that GO could be effectively reduced to graphene during the hydrothermal process.<sup>30,31,34,40</sup>

To evaluate the polysulfide-adsorption capability, the as-prepared SnS<sub>2</sub>-ND@G aerogel was immersed into a pure polysulfide (Li<sub>2</sub>S<sub>6</sub>) solution. A graphene aerogel was also immersed into

the same solution as a control. The comparison is shown in Fig. 4c. The  $\text{Li}_2\text{S}_6$  solution changes color from yellow to almost transparent after adding the  $\text{SnS}_2\text{-ND@G}$  aerogel; in sharp contrast, the  $\text{Li}_2\text{S}_6$  solution remains a visible yellow color with the addition of only graphene aerogel. The concentration variations of the residual  $\text{Li}_2\text{S}_6$  solutions of both samples and the original  $\text{Li}_2\text{S}_6$  solution were then quantitatively analyzed with ultraviolet–visible (UV-vis) absorption spectroscopy (Fig. 4d). The characteristic peaks of  $\text{Li}_2\text{S}_6$  solution located at 260, 280, 300, and 340 nm are attributed to the  $\text{S}_6^{2-}$  species.<sup>40</sup> It is demonstrated that the intensity of these  $\text{S}_6^{2-}$  absorption peaks declines slightly in the residual solution collected from the  $\text{Li}_2\text{S}_6$  solution with graphene aerogel, as a result of weak physical polysulfide-absorption on graphene. In striking contrast, the residual solution collected from the  $\text{Li}_2\text{S}_6$  solution with  $\text{SnS}_2\text{-ND@G}$  aerogel shows a significant decrease in the peak intensity, implying a strong chemical adsorption of  $\text{SnS}_2$  towards polysulfides.<sup>26,40</sup> Furthermore, such a chemical interaction is further reflected in the XPS analysis (Fig. 4e). In the high-resolution Sn 3d spectrum of fresh  $\text{SnS}_2\text{-ND@G}$  aerogel, the peaks centered at 487.1 and 495.6 eV are ascribed to the  $3d_{5/2}$  and  $3d_{3/2}$  peaks of  $\text{Sn}^{4+}$  in  $\text{SnS}_2$ .<sup>30,31,34,41</sup> After contacting with the  $\text{Li}_2\text{S}_6$  solution, both the  $3d_{5/2}$  and  $3d_{3/2}$  peaks shift towards lower binding energies. Meanwhile, the Li 1s spectrum of pristine  $\text{Li}_2\text{S}_6$  depicts a Li–S peak at 56.3 eV, and this peak negatively shifts to 56.1 eV after contacting with  $\text{SnS}_2\text{-ND@G}$  (Fig. 4f). Both peak shifts in Sn 3d and Li 1s suggest the formation of chemical bonds between  $\text{SnS}_2$  and  $\text{Li}_2\text{S}_6$ .<sup>15,17,18,26,42</sup> These analytical results indicate that  $\text{SnS}_2\text{-ND@G}$  aerogel exhibits prominent polysulfide-trapping ability owing to the synergy between physical absorption and chemical adsorptivity towards polysulfides.<sup>15,21</sup>

Fig. 5a depicts the cyclic voltammetry (CV) profiles of the Li-S cell employing the  $\text{SnS}_2\text{-ND@G}$  aerogel cathode at a scan rate of  $0.05 \text{ mV s}^{-1}$  under the voltage window of 1.7 – 2.8 V. It

demonstrates a typical two-step redox reaction. The first cathodic peak at  $\sim 2.35$  V (marked as C1) and the second one at  $\sim 2.05$  V (marked as C2) represent, respectively, the transition from elemental sulfur to polysulfides and then to sulfide mixtures ( $\text{Li}_2\text{S}_2/\text{Li}_2\text{S}$ ).<sup>35,43</sup> And the continuous anodic peak at  $2.41 \sim 2.45$  V (marked as A1) corresponds to the reversible conversion from  $\text{Li}_2\text{S}_2/\text{Li}_2\text{S}$  to  $\text{Li}_2\text{S}_8/\text{S}$ .<sup>14,35</sup> Fig. 5b displays the charge/discharge curves of the Li-S cell with  $\text{SnS}_2\text{-ND@G}$  aerogel cathode. The two separated upper and lower-discharge plateaus and two incessant charge plateaus confirm the two-step redox reaction shown in the CV profiles.<sup>44,45</sup> In addition, the polarization value obtained from the charge/discharge curves at C/5 rate is  $\sim 0.29$  V. It is noted that the CV and charge/discharge curves both demonstrate superior electrochemical accessibility and redox-conversion reversibility, as evidenced by the overlapping sharp CV peaks and well-preserved charge/discharge plateaus during repeated cycling.<sup>14,29,35,46</sup> Furthermore, the enhanced electrochemical redox kinetics is further validated by the result of the galvanostatic intermittent titration technique (GITT) on the  $\text{SnS}_2\text{-ND@G}$  aerogel. The GITT profiles were obtained by adding a constant current of C/15 for 1 h, followed by a resting step in the absence of current for another 1 h. Fig. 5c detects only slight changes in voltages ( $\sim 0.03$  V) upon removing the current, indicating a promoted electrochemical stability and reversible redox-reaction capability.<sup>47</sup> It should be noted that as the cycling rate declines to C/15, the polarization value of the cell is significantly decreased to  $\sim 0.19$  V. Moreover, the electrochemical impedance spectroscopy (EIS) measurements in Fig. 5d display low cell resistance of the Li-S cell equipped with the  $\text{SnS}_2\text{-ND@G}$  cathode before and after cycling, further confirming the improved electrochemical kinetics in the hybrid aerogel architecture.<sup>43,48,49</sup>

On the other hand, the electrochemical behavior is also reflected in the changes of the upper-plateau discharge capacity ( $Q_{\text{H}}$ , theoretical value:  $419 \text{ mA h g}^{-1}$ ) and lower-plateau discharge

capacity ( $Q_L$ , theoretical value:  $1256 \text{ mA h g}^{-1}$ ). Both electrochemical parameters are investigated as quantitative indicators for, respectively, the level of polysulfide-trapping ability and the accessibility of redox reaction of the cells.<sup>14,29,35</sup> In Fig. 5e, at C/5 rate, the Li-S cell utilizing the SnS<sub>2</sub>-ND@G aerogel cathode delivers an initial  $Q_H$  of as high as  $390 \text{ mA h g}^{-1}$ , achieving a  $Q_H$  utilization up to 93%. After 300 cycles, the cell still delivers a high  $Q_H$  value of  $250 \text{ mA h g}^{-1}$ , corresponding to a  $Q_H$  retention rate ( $R_{QH}$ ) of 64%. Meanwhile, Fig. 5f displays a high initial  $Q_L$  of  $844 \text{ mA h g}^{-1}$  in the Li-S cell employing the SnS<sub>2</sub>-ND@G aerogel cathode, and the  $Q_L$  value is retained at  $766 \text{ mA h g}^{-1}$  after 300 cycles, representing a high  $Q_L$  retention rate ( $R_{QL}$ ) of up to 91%. In sharp contrast, the control cell fabricated with pristine graphene cathode suffers from rapid capacity fade, leading to much lower  $R_{QH}$  (24%) and  $R_{QL}$  (35%) values after 250 cycles. Such quantitative comparison analytically evidences the greatly limited polysulfide diffusion and highly improved electrochemical reactivity contributed by the SnS<sub>2</sub>-ND@G aerogel architecture.<sup>14,35</sup>

Fig. 6a demonstrates the long-term cycling performance of the Li-S cells with a sulfur loading of  $2.5 \text{ mg cm}^{-2}$ . At C/5 rate, the SnS<sub>2</sub>-ND@G aerogel approaches a peak discharge capacity of  $1234 \text{ mA h g}^{-1}$ . After 300 cycles, the discharge capacity is still stabilized at  $1016 \text{ mA h g}^{-1}$ , representing a high capacity retention of 82% and a low capacity-fading rate of 0.06% per cycle. In striking contrast, after 250 cycles, the control cell ends up with a discharge capacity of  $360 \text{ mA h g}^{-1}$  which is over three times lower than that with SnS<sub>2</sub>-ND@G aerogel. Such a low remaining discharge capacity in the control cell is accompanied by low capacity retention (32%) and fast capacity decay (0.3% per cycle), resulting in limited polysulfide-retention ability and short cycle life. Notably, the Coulombic efficiency drop during long cycles could be ascribed to the irreversible consumption of LiNO<sub>3</sub> in the electrolyte.<sup>50</sup> Moreover, the SnS<sub>2</sub>-ND@G aerogel also renders considerable enhancement in rate performance, as evidenced by higher capacity and better

electrochemical stability under varied cycling rates. ( $C/10 - 3C$  rates). As shown in Fig. 6b, at  $C/10$ ,  $C/5$ ,  $C/3$ ,  $C/2$ ,  $1C$ , and  $2C$  rates, the Li-S cell employing the  $\text{SnS}_2\text{-ND@G}$  aerogel cathode delivers high discharge capacities of, respectively, 1263, 1042, 870, 650, 514, and 412  $\text{mA h g}^{-1}$ , advantageously outperforming the rate capability of the control cell. Even at  $3C$  rate, the discharge capacity of  $\text{SnS}_2\text{-ND@G}$  still remains at 350  $\text{mA h g}^{-1}$ , remarkably exceeding the control cell with no observable discharge capacity. Such comparative results clearly validate that the  $\text{SnS}_2\text{-ND@G}$  aerogel cathode has more pronounced effect on suppressing polysulfide diffusion and minimizing the active-material loss, contributing to the greatly improved electrochemical utilization and stable cyclability of cells.

Furthermore, the superiority of the  $\text{SnS}_2\text{-ND@G}$  aerogel configuration as a cathode substrate could be further extended to higher sulfur loading, as illustrated in Fig. 6c. At  $C/5$  rate, loaded with 6 and 10  $\text{mg cm}^{-2}$  sulfur, the  $\text{SnS}_2\text{-ND@G}$  cathode is able to reach discharge capacities of, respectively, 1120 and 1133  $\text{mA h g}^{-1}$ . Note that the initial drop in the capacity is mainly attributed to the  $\text{LiNO}_3$  decomposition and the formation of a solid electrolyte interface (SEI) film.<sup>40</sup> After 100 cycles, the reversible discharge capacities maintain, respectively, at 750 and 816  $\text{mA h g}^{-1}$ , achieving a high capacity retention stabilized at  $\sim 70\%$ . Additionally, the corresponding areal capacity could achieve up to 11  $\text{mA h cm}^{-2}$  and sustain around 6  $\sim$  8  $\text{mA h cm}^{-2}$  during 100 cycles (Fig. 6d). As a reference, the current commercial Li-ion cell has an areal capacity of 4  $\text{mA h cm}^{-2}$ .<sup>14</sup> As a result, this well-designed  $\text{SnS}_2\text{-ND@G}$  aerogel cathode structure exhibits excellent polysulfide-retention capability and electrochemical stability, enabling the high sulfur-loading cathode to achieve impressive cell performance.

## Conclusions

In summary, we have established a novel self-assembled graphene aerogel incorporated with *in-situ* deposited SnS<sub>2</sub> nano dots (SnS<sub>2</sub>-ND@G) as an efficient sulfur host. Benefiting from the synergistic effect of physical and chemical interaction with polysulfides, the porous conductive SnS<sub>2</sub>-ND@G aerogel architecture exhibits significantly improved polysulfide-trapping capability and redox-conversion reversibility. With a high sulfur content and loading (75 wt.% and 2.5 mg cm<sup>-2</sup>), the cell shows a high peak discharge capacity of 1234 mA h g<sup>-1</sup>, a high capacity retention (82%) after 300 cycles, and superior rate capability (C/10 – 3C rates). Furthermore, even equipped with a higher sulfur loading (up to 10 mg cm<sup>-2</sup>), the SnS<sub>2</sub>-ND@G aerogel cathode still achieves a high discharge capacity of 1133 mA h g<sup>-1</sup>, corresponding to an areal capacity of up to 11 mA h cm<sup>-2</sup>. This work demonstrates that the combination of graphene substrate and metal sulfides with nano structure has the potential to be reliable cathodes for high-performance Li-S batteries.

## Acknowledgements

This work was supported by the Department of Energy (DOE), Office of Energy Efficiency and Renewable Energy (EERE), under Award Number DE-EE0007218.

**Notes and references**

- 1 A. Manthiram, S.-H. Chung and C. Zu, *Adv. Mater.*, 2015, **27**, 1980-2006.
- 2 R. Fang, S. Zhao, Z. Sun, D. W. Wang, H. M. Cheng and F. Li, *Adv. Mater.*, 2017, **29**, 1606823.
- 3 Q. Pang, X. Liang, C. Y. Kwok and L. F. Nazar, *Nat. Energy*, 2016, **1**, 16132.
- 4 A. Manthiram, Y. Fu and Y.-S. Su, *Acc. Chem. Res.*, 2013, **46**, 1125-1134.
- 5 N. Xu, T. Qian, X. Liu, J. Liu, Y. Chen and C. Yan, *Nano Lett.*, 2017, **17**, 538-543.
- 6 J. Liu, T. Qian, M. Wang, X. Liu, N. Xu, Y. You and C. Yan, *Nano Lett.*, 2017, **17**, 5064-5070.
- 7 J. Zhou, T. Qian, N. Xu, M. Wang, X. Ni, X. Liu, X. Shen and C. Yan, *Adv. Mater.*, 2017, **29**, 1701294.
- 8 A. Manthiram, Y. Fu, S.-H. Chung, C. Zu and Y.-S. Su, *Chem. Rev.*, 2014, **114**, 11751-11787.
- 9 H. Chen, C. Chen, Y. Liu, X. Zhao, N. Ananth, B. Zheng, L. Peng, T. Huang, W. Gao and C. Gao, *Adv. Energy Mater.*, 2017, **7**, 1700051.
- 10 L. Fei, X. Li, W. Bi, Z. Zhuo, W. Wei, L. Sun, W. Lu, X. Wu, K. Xie, C. Wu, H. L. Chan and Y. Wang, *Adv. Mater.*, 2015, **27**, 5936-5942.
- 11 J. Q. Huang, Z. Wang, Z. L. Xu, W. G. Chong, X. Qin, X. Wang and J. K. Kim, *ACS Appl. Mater. Interfaces*, 2016, **8**, 28663-28670.
- 12 G. Zhou, S. Pei, L. Li, D. W. Wang, S. Wang, K. Huang, L. C. Yin, F. Li and H. M. Cheng, *Adv. Mater.*, 2014, **26**, 625-631.
- 13 B. Luo, Y. Fang, B. Wang, J. Zhou, H. Song and L. Zhi, *Energy Environ. Sci.*, 2012, **5**, 5226-5230.
- 14 L. Luo, S.-H. Chung, C.-H. Chang and A. Manthiram, *J. Mater. Chem. A*, 2017, **5**, 15002-15007.
- 15 J. He, L. Luo, Y. Chen and A. Manthiram, *Adv. Mater.*, 2017, **29**, 1702707.

- 16 Z. Li, J. Zhang, B. Guan, D. Wang, L. M. Liu and X. W. Lou, *Nat. Commun.*, 2016, **7**, 13065.
- 17 Q. Pang, D. Kundu, M. Cuisinier and L. F. Nazar, *Nat. Commun.*, 2014, **5**, 4759.
- 18 X. Liang, C. Hart, Q. Pang, A. Garsuch, T. Weiss and L. F. Nazar, *Nat. Commun.*, 2015, **6**, 5682.
- 19 R. Ponraj, A. G. Kannan, J. H. Ahn and D. W. Kim, *ACS Appl. Mater. Interfaces*, 2016, **8**, 4000-4006.
- 20 X. Liang, C. Y. Kwok, F. Lodi-Marzano, Q. Pang, M. Cuisinier, H. Huang, C. J. Hart, D. Houtarde, K. Kaup, H. Sommer, T. Brezesinski, J. Janek and L. F. Nazar, *Adv. Energy Mater.*, 2016, **6**, 1501636.
- 21 Z. Yuan, H. J. Peng, T. Z. Hou, J. Q. Huang, C. M. Chen, D. W. Wang, X. B. Cheng, F. Wei and Q. Zhang, *Nano Lett.*, 2016, **16**, 519-527.
- 22 Z. W. Seh, J. H. Yu, W. Li, P. C. Hsu, H. Wang, Y. Sun, H. Yao, Q. Zhang and Y. Cui, *Nat. Commun.*, 2014, **5**, 5017.
- 23 Y.-S. Su and A. Manthiram, *J. Power Sources*, 2014, **270**, 101-105.
- 24 X. Li, K. Hu, R. Tang, K. Zhao and Y. Ding, *RSC Adv.*, 2016, **6**, 71319-71327.
- 25 D. Liu, C. Zhang, G. Zhou, W. Lv, G. Ling, L. Zhi and Q.-H. Yang, *Adv. Sci.*, 2017, **5**, 1700270.
- 26 G. Zhou, H. Tian, Y. Jin, X. Tao, B. Liu, R. Zhang, Z. W. Seh, D. Zhuo, Y. Liu, J. Sun and J. Zhao, *Proc. Natl. Acad. Sci.*, 2017, **114**, 840-845.
- 27 J. He, Y. Chen, W. Lv, K. Wen, Z. Wang, W. Zhang, Y. Li, W. Qin and W. He, *ACS Nano*, 2016, **10**, 8837-8842.
- 28 S.-H. Chung, C.-H. Chang and A. Manthiram, *Energy Environ. Sci.*, 2016, **9**, 3188-3200.
- 29 S.-H. Chung, C.-H. Chang and A. Manthiram, *ACS Nano*, 2016, **10**, 10462-10470.

- 30 L. Zhang, Y. Huang, Y. Zhang, W. Fan and T. Liu, *ACS Appl. Mater. Interfaces*, 2015, **7**, 27823-27830.
- 31 X. Jiang, X. Yang, Y. Zhu, J. Shen, K. Fan and C. Li, *J. Power Sources*, 2013, **237**, 178-186.
- 32 K. Chang, Z. Wang, G. Huang, H. Li, W. Chen and J. Y. Lee, *J. Power Sources*, 2012, **201**, 259-266.
- 33 N. Du, X. Wu, C. Zhai, H. Zhang and D. Yang, *J. Alloys Compd.*, 2013, **580**, 457-464.
- 34 S. Liu, X. Lu, J. Xie, G. Cao, T. Zhu and X. Zhao, *ACS Appl. Mater. Interfaces*, 2013, **5**, 1588-1595.
- 35 L. Luo and A. Manthiram, *ACS Energy Lett.*, 2017, **2**, 2205-2211.
- 36 Q. Zhang, R. Li, M. Zhang, B. Zhang and X. Gou, *Electrochim. Acta*, 2014, **115**, 425-433.
- 37 B. Qu, C. Ma, G. Ji, C. Xu, J. Xu, Y. S. Meng, T. Wang and J. Y. Lee, *Adv. Mater.*, 2014, **26**, 3854-3859.
- 38 Y. Du, Z. Yin, X. Rui, Z. Zeng, X. J. Wu, J. Liu, Y. Zhu, J. Zhu, X. Huang, Q. Yan and H. Zhang, *Nanoscale*, 2013, **5**, 1456-1459.
- 39 K. S. W. Sing, D. H. Everett, R. A. W. Haul, L. Moscou, R. A. Pierotti, J. Rouquerol and T. Siemieniowska, *Pure & Appl. Chem.*, 1985, **57**, 603-619.
- 40 G. Zhou, E. Paek, G. S. Hwang and A. Manthiram, *Nat. Commun.*, 2015, **6**, 7760.
- 41 M. Sathish, S. Mitani, T. Tomai and I. Honma, *J. Phys. Chem. C*, 2012, **116**, 12475-12481.
- 42 J. Pu, Z. Shen, J. Zheng, W. Wu, C. Zhu, Q. Zhou, H. Zhang and F. Pan, *Nano Energy*, 2017, **37**, 7-14.
- 43 L. Luo, S.-H. Chung and A. Manthiram, *J. Mater. Chem. A*, 2016, **4**, 16805-16811.
- 44 C.-H. Chang, S.-H. Chung, P. Han and A. Manthiram, *Mater. Horiz.*, 2017, **4**, 908-914.
- 45 C.-H. Chang, S.-H. Chung and A. Manthiram, *Mater. Horiz.*, 2017, **4**, 249-258.

- 46 S.-H. Chung and A. Manthiram, *Adv. Mater.*, 2014, **26**, 1360-1365.
- 47 L. Qie and A. Manthiram, *ACS Energy Lett.*, 2016, **1**, 46-51.
- 48 H. Lin, L. Yang, X. Jiang, G. Li, T. Zhang, Q. Yao, G. W. Zheng and J. Y. Lee, *Energy Environ. Sci.*, 2017, **10**, 1476-1486.
- 49 Q. Pang, D. Kundu and L. F. Nazar, *Mater. Horiz.*, 2016, **3**, 130-136.
- 50 Y.-S. Su, Y. Fu, T. Cochell and A. Manthiram, *Nat. Commun.*, 2013, **4**, 2985.

## Figures

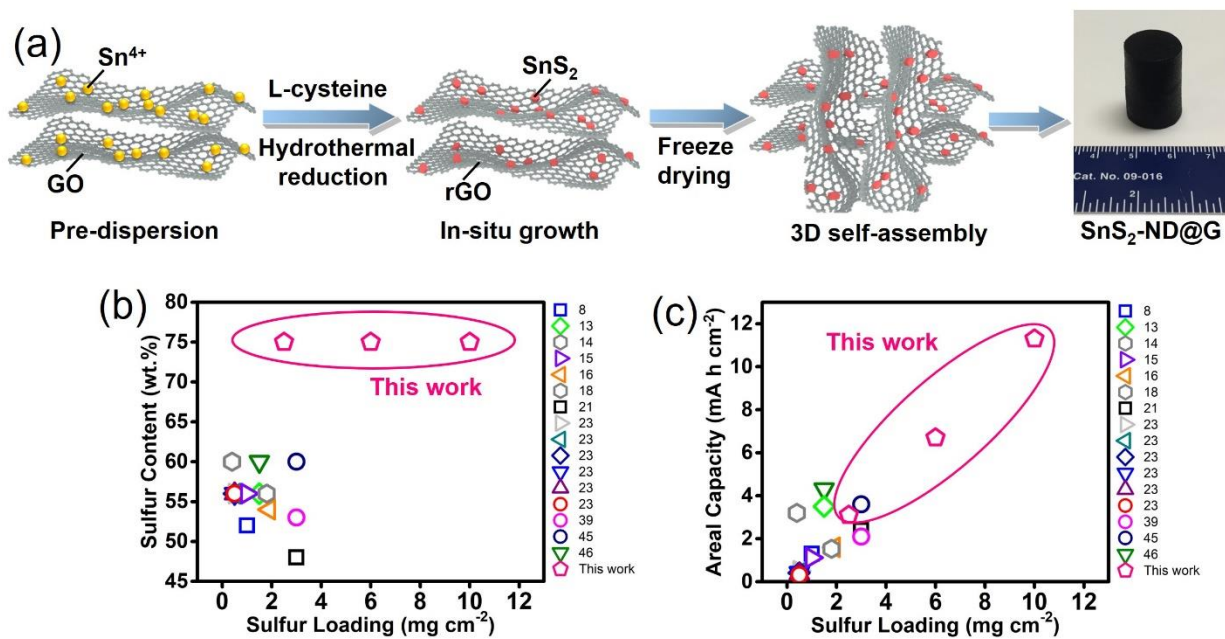


**Fig. 1** (a) Schematic illustration of the fabrication procedure and digital photo of the SnS<sub>2</sub>-ND@G aerogel. (b) and (c) Comparative analyses of the cell parameters in this work and other reported studies involving metal-sulfide/carbon and other metal compounds as sulfur cathodes.

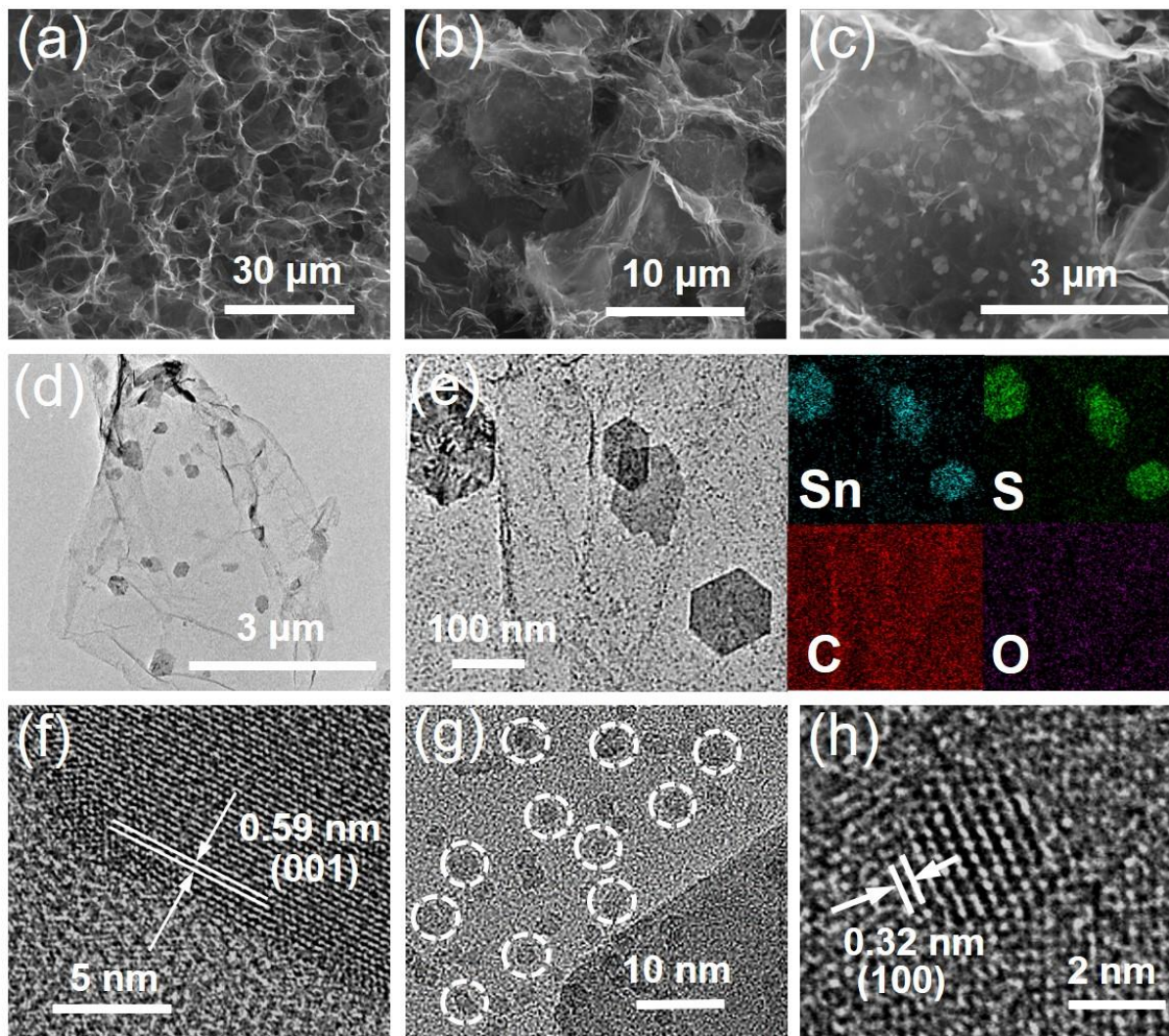


**Fig. 2** (a – c) SEM images of SnS<sub>2</sub>-ND@G aerogel. (d) and (e) TEM images of SnS<sub>2</sub>-ND@G aerogel and corresponding EDX elemental mapping results. (f – h) HRTEM images of SnS<sub>2</sub> nano dots in the SnS<sub>2</sub>-ND@G aerogel.

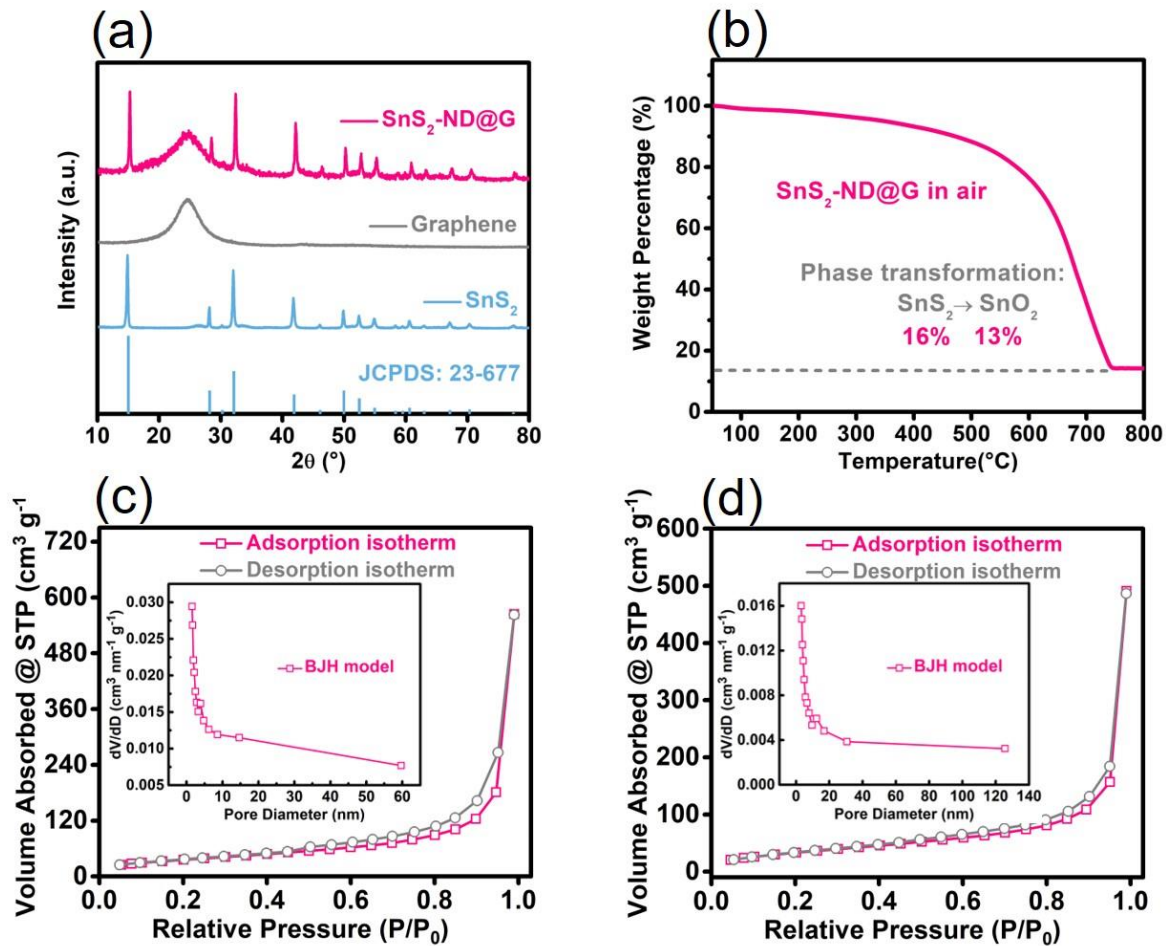


**Fig. 3** (a) XRD patterns of pristine SnS<sub>2</sub>, graphene, and SnS<sub>2</sub>-ND@G aerogel. (b) TGA curve of SnS<sub>2</sub>-ND@G aerogel in air. Isotherms and pore-size distribution by the Barrett-Joyner-Halenda (BJH) method: (c) SnS<sub>2</sub>-ND@G and (d) graphene aerogels.

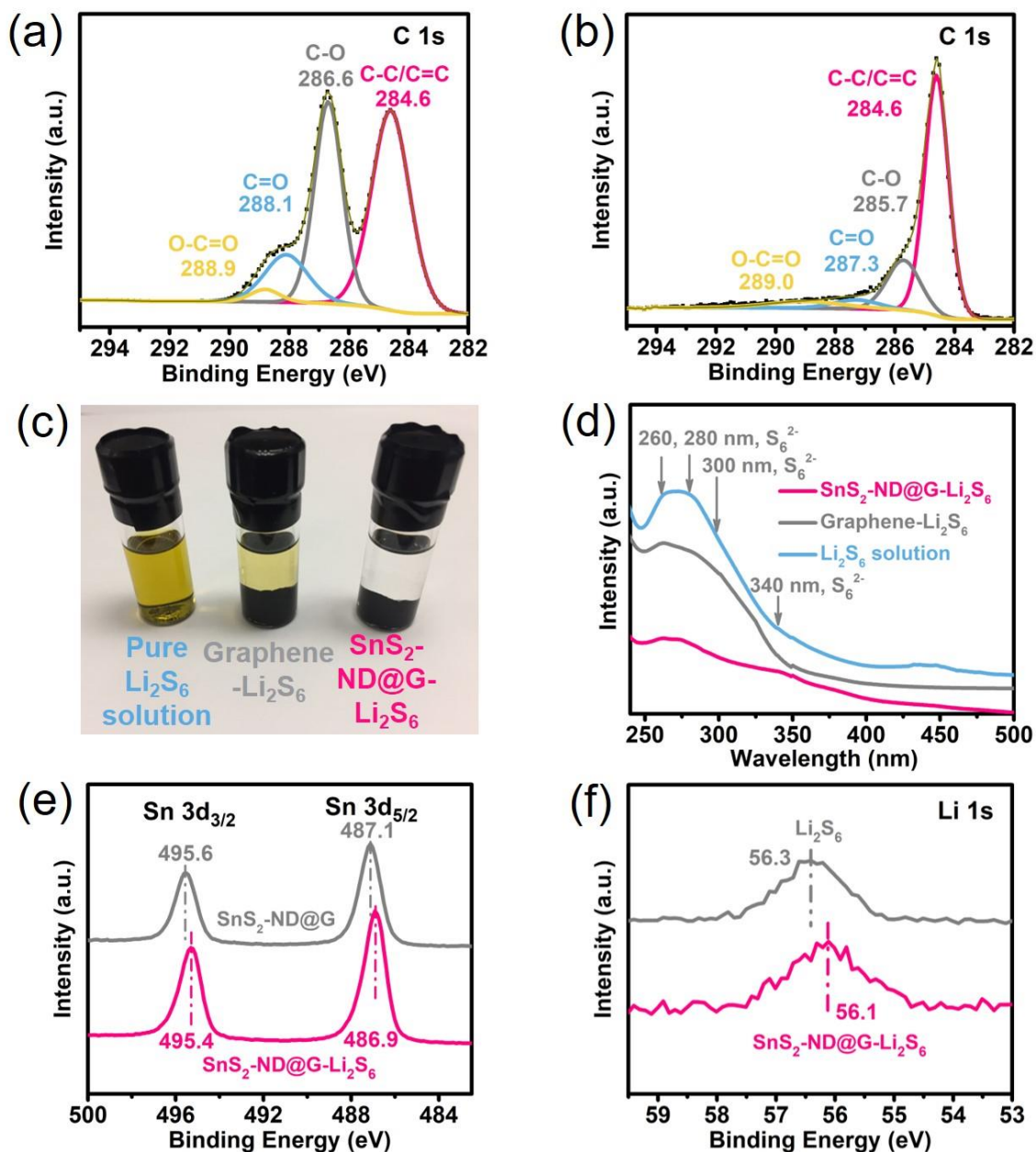


**Fig. 4** C 1s XPS spectra of (a) GO and (b) SnS<sub>2</sub>-ND@G aerogel. (c) Digital photo of polysulfide (Li<sub>2</sub>S<sub>6</sub>) adsorption by graphene and SnS<sub>2</sub>-ND@G aerogel and (d) corresponding UV-vis absorption spectroscopy of the residual Li<sub>2</sub>S<sub>6</sub> solution. (e) Sn 3d XPS spectra of SnS<sub>2</sub>-ND@G aerogel before (gray line) and after (pink line) contacting with Li<sub>2</sub>S<sub>6</sub> solution. (f) Li 1s XPS spectra of the as-prepared Li<sub>2</sub>S<sub>6</sub> solution (gray line) and the residual Li<sub>2</sub>S<sub>6</sub> solution after contacting with the SnS<sub>2</sub>-ND@G aerogel (pink line).

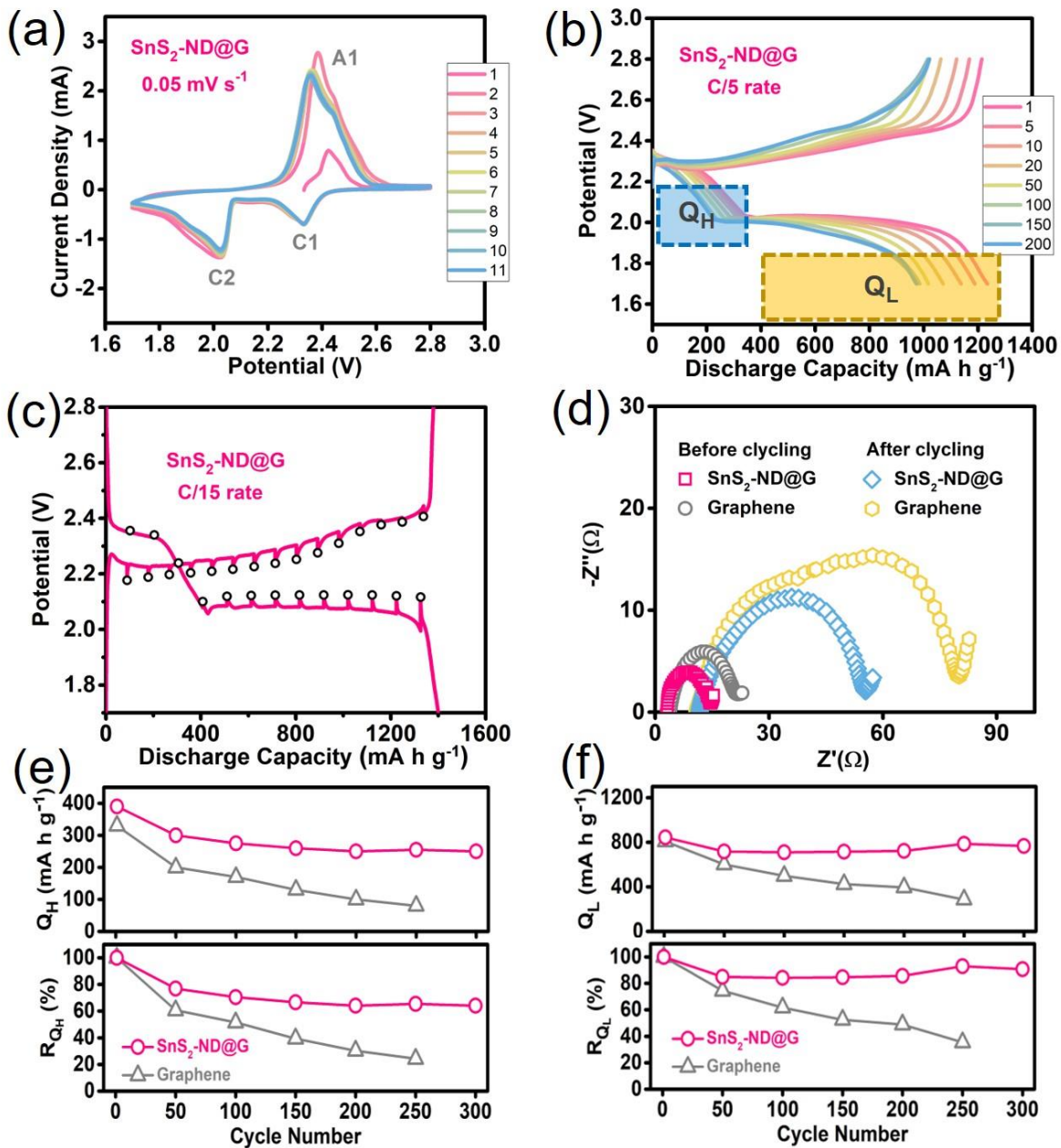


**Fig. 5** (a) CV plots and (b) charge/discharge profiles of the cell with the SnS<sub>2</sub>-ND@G cathode. (c) GITT curves of the cell employing the SnS<sub>2</sub>-ND@G cathode. The voltage at the end of the relaxation is marked with a black circle. (d) EIS spectra of the fresh and cycled cells employing SnS<sub>2</sub>-ND@G and graphene cathodes. (e) Q<sub>H</sub>/R<sub>QH</sub> and (f) Q<sub>L</sub>/R<sub>QL</sub> analyses.

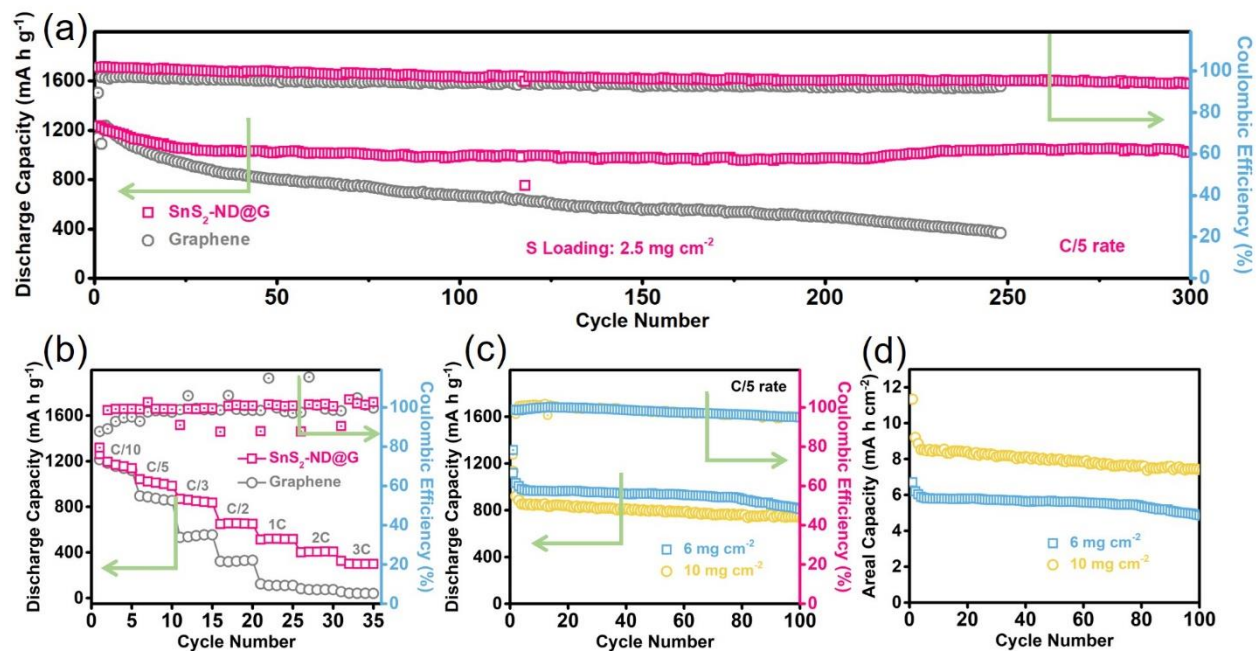


**Fig. 6** (a) Long-term cycling and (b) rate performances of the cells with SnS<sub>2</sub>-ND@G and graphene cathodes. Cycling performance of the cells employing the SnS<sub>2</sub>-ND@G cathodes with higher sulfur loadings: (c) discharge capacities and (d) areal capacities.